

Tunable Fano resonance in photonic crystal slabs

Junfeng Song

Institute of Microelectronics, 11 Science Park Road, Science Park II, Singapore 117685
School of Electronic and Electrical engineering, Nanyang Technological University, Nanyang Avenue, Singapore 639798
State Key Laboratory on Integrated Opto-electronics, College of Electronic Science and Engineering, Jilin University, Changchun, 130023 People's Republic of China
Institute of Semiconductors of Chinese Academy of Sciences, 100083, People's Republic of China
songjf@ime.a-star.edu.sg

Remo Proietti Zaccaria

LaSIE, Department of Applied Physics Osaka University, 2-1 Yamada-Oka, Suita, Osaka 565-0871, Japan
Magna Graecia University, BIONEM laboratory, Campus Germaneto, Viale Europa, 88100 Catanzaro, Italy

M. B. Yu

Institute of Microelectronics, 11 Science Park Road, Science Park II, Singapore 117685

X. W. Sun

School of Electronic and Electrical engineering, Nanyang Technological University, Nanyang Avenue, Singapore 639798
Institute of Microelectronics, 11 Science Park Road, Science Park II, Singapore 117685
EXWSun@ntu.edu.sg

Abstract: A three dimensional analysis of a special class of anisotropic materials is presented. We introduce an extension of the Scattering Matrix Method (SMM) to investigate the behavior of anisotropic Photonic Crystal Slabs (PhCS) subject to external radiation. We show how the Fano effect can play a fundamental role in the realization of tunable optical devices. Moreover, we show how to utilize electron injection, electric field and temperature as parameters to control the Fano resonance shift in both isotropic and anisotropic materials as Si and Potassium Titanium Oxide Phosphate (KTP). We will see that because Fano modes are sensitive and controllable, a broad range of applications can be considered.

©2006 Optical Society of America

OCIS codes: (230.7400) Waveguides, slab; (250.5300) Photonic integrated circuits; (050.1950) Diffraction gratings

References and links

1. Jakob S. Jensen and Ole Sigmund, "Systematic design of photonic crystal structures using topology optimization: Low-loss waveguide bends," *Appl. Phys. Lett.* **84**, 2021-2023 (2004).
2. Akihiko Shinya, Satoshi Mitsugi, Eiichi Kuramochi, and Masaya Notomi "Ultrasmall multi-channel resonant-tunneling filter using mode gap of width-tuned photonic crystal waveguide," *Opt. Express* **13**, 4202-4209 (2005).
3. L. H. Frandsen, P. I. Borel, Y. X. Zhuang, A. Harpøth, M. Thorhauge, M. Kristensen, W. Bogaerts, P. Dumon, R. Baets, V. Wiaux, J. Wouters, and S. Beckx, "Ultralow-loss 3-dB photonic crystal waveguide splitter," *Opt. Lett.* **29**, 1623-1625 (2004).
4. X. Checoury, P. Boucaud, J-M. Lourtioz, F. Pommereau, C. Cuisin, E. Derouin, O. Drisse, L. Legouezigou, F. Lelarge, F. Poingt, G. H. Duan, D. Mulin, S. Bonnefont, O. Gauthier-Lafaye, J. Valentin, F. Lozes, A. Talneau, "Distributed feedback regime of photonic crystal waveguide lasers at 1.5 μm ," *Appl. Phys. Lett.* **85**, 5502-5504 (2004).

5. Yongqiang Jiang, Wei Jiang, Lanlan Gu, Xiaonan Chen, and Ray T. Chen, "80-micron interaction length silicon photonic crystal waveguide modulator," *Appl. Phys. Lett.* **87**, 221105-221107 (2005).
6. Shanhui Fan and J. D. Joannopoulos, "Analysis of guided resonances in photonic crystal slabs," *Phys. Rev. B* **65**, 235112 (2002).
7. S. G. Tikhodeev, A. L. Yablonskii, E. A. Muljarow, N. A. Gippius, and Teruya Ishihara, "Quasiguide modes and optical properties of photonic crystal slabs," *Phys. Rev. B* **66**, 045102 (2002).
8. Steven G. Johnson, Shanhui Fan, Pierre R. Villeneuve, J. D. Joannopoulos, and L. A. Kolodziejski, "Guided modes in photonic crystal slabs," *Phys. Rev. B* **60**, 5751-5758 (1999).
9. K. B. Crozier, Virginie Lousse, Onur Kilic, Sora Kim, Shanhui Fan, and Olav Solgaard, "Air-bridged photonic crystal slabs at visible and near-infrared wavelength," *Phys. Rev. B* **73**, 115126 (2006).
10. Vasily N. Astratov, Ian S. Culshaw, R. Mark Stevenson, David M. Whittaker, Maurice S. Skolnick, Thomax F. Krauss, Richard M. De La Rue, "Resonant coupling of near-infrared radiation to photonic band structure waveguide," *J. Lightwave Technol.* **17**, 2050-2057 (1999).
11. V. N. Astratov, R. M. Stevenson, I. S. Culshaw, D. M. Whittaker, M.S. Skolnick, T.F. Krauss and R. M. De La Rue, "Heavy photon dispersions in photonic crystal waveguides," *Appl. Phys. Lett.* **77**, 178-180 (2000).
12. A. Rosenberg, Michael W. Carter, J. A. Casey, Mijin Kim, Ronald T. Holm, Richard L. Henry, Charles R. Eddy, V. A. Shamamian, K. Bussmann Shouyuan Shi, Dennis W. Prather, "Guided resonances in symmetrical GaN photonic crystal slabs observed in the visible spectrum," *Opt. Express* **13**, 6564-6571 (2005).
13. Andrey E. Miroshnichenko and Yuri S. Kivshar, "Sharp bends in photonic crystal waveguides as nonlinear Fano resonators," *Opt. Express* **13**, 3969-3976 (2005).
14. David Yuk Kei Ko and J. C. Inkson, "Matrix method for tunneling in heterostructures: Resonant tunneling in multilayer systems," *Phys. Rev. B* **38**, 9945-9951 (1988).
15. D. M. Whittaker and I. S. Culshaw, "Scattering-matrix treatment of patterned multilayer photonic structures," *Phys. Rev. B* **60**, 2610-2618 (1999).
16. Maciej Dems, Rafal Kotynski and Krassimir Panajotov, "Plane wave admittance method-a novel approach for determining the electromagnetic modes in photonic structures," *Opt. Express* **13**, 3196-3207 (2005).
17. R. A. Soref, and B. R. Bennett "Electro-optical Effects in Silicon," *IEEE J. Quantum Electron.* **23**, 123-129 (1987).
18. A. Irace, G. Breglio, and A. Cutolo, "All-silicon optoelectronic modulator with 1 GHz switching capability," *Electron. Lett.* **39**, 232-233 (2003).
19. R.W. Wood, "Anomalous Diffraction Gratings," *Phys. Rev.* **48**, 928-936 (1935).
20. U. Fano, "The Theory of Anomalous Diffraction Gratings and of Quasi-Stationary Waves on Metallic Surfaces (Sommerfeld's Waves)," *J. Opt. Soc. Am.* **31**, 213-222 (1941).
21. U. Fano, "Effect of Configuration Interaction on Intensity and Phase Shifts," *Phys. Rev.* **124**, 1866-1878 (1961).
22. A. Hessel and A.A. Oliner, "A New Theory of Wood's Anomalies on Optical Gratings," *Appl. Opt.* **4**, 1275-1297 (1965).
23. T.W. Ebbesen, H.J. Lezec, H.F. Ghaemi, T. Thio, and P.A. Wolff, "Extraordinary optical transmission through sub-wavelength hole arrays," *Nature* **391**, 667-669 (1998).
24. E. Popov, M. Nevière, S. Enoch, and R. Reinisch, "Theory of light transmission through subwavelength periodic hole arrays," *Phys. Rev. B* **62**, 16100-16108 (2000).
25. M.G. Banaee, A.R. Cowan, and J.F. Young, "Third-order nonlinear influence on specular reflectivity of two-dimensional waveguide-based photonic crystals," *J. Opt. Soc. Am. B* **19**, 2224 (2002).
26. M. Sarrazin, J.P. Vigneron, and J.M. Vigoureux, "Role of Wood anomalies in optical properties of thin metallic films with bidimensional array of subwavelength holes," *Phys. Rev. B* **67**, 085415 (2003).
27. J.M. Steele, C.E. Moran, A. Lee, C.M. Aguirre, and N.J. Halas, "Metallo-dielectric gratings with subwavelength slots: Optical properties," *Phys. Rev. B* **68**, 205103 (2003).
28. W.L. Barnes, W.A. Murray, J. Dintinger, E. Devaux, and T.W. Ebbesen, "Surface Plasmon Polaritons and Their Role in the Enhanced Transmission of Light through Periodic Arrays of Subwavelength Holes in a Metal Film," *Phys. Rev. Lett.* **92**, 107401 (2004).
29. W.V. Lousse and J.P. Vigneron, "Use of Fano resonances for bistable optical transfer through photonic crystal film," *Phys. Rev. B* **69**, 155106 (2004).
30. H.J. Lezec and T. Thio, "Diffracted evanescent wave model for enhanced and suppressed optical transmission through subwavelength hole arrays," *Opt. Express* **12**, 3629-3651 (2004).
31. A.E. Miroshnichenko and Y.S. Kivshar, "Engineering Fano resonances in discrete arrays," *Phys. Rev. E* **72**, 056611 (2005).
32. E. Moreno, L. Martin-Moreno, and F.J. Garcia-Vidal, "Extraordinary optical transmission without plasmons: the s-polarization case," *J. Opt. A: Pure Appl. Opt.* **8**, S94-S97 (2006).
33. R. Gomez-Medina, M. Laroche, and J.J. Saenz, "Extraordinary optical reflection from sub-wavelength cylinder arrays," *Opt. Express* **14**, 3730-3737 (2006).

34. B. Boulanger, J.P. Feve, and Y. Guillian, "Thermo-optical effect and saturation of nonlinear absorption induced by gray tracking in a 532-nm pumped KTP optical parametric oscillator," Opt. Lett. **25**, 484-486 (2000).
-

1. Introduction

Photonic Crystal Slab (PhCS) represents the fundamental structure for photon integration circuits. Many devices have an architecture based on PhCS, such as waveguides, filters, splitters, modulators and lasers [1-5]. The basic idea is to utilize the characteristic band gap or dispersion relation of PhCS to get the desired device performances. For example, waveguides support *guided modes* that are *confined* in the slab plane, with no possibility to interact with any external radiation.

Because of their potential applications, PhCS have been recently attracting more attention, as testify by the number of publications in the field [6-9]. An important and interesting phenomenon which can occur in PhCS is Fano resonance. This effect manifests itself when incoming light can couple a discrete state with a continuum of states. Astratov *et al.* [10,11] measured reflection spectra of one and two dimensional PhCS, showing sharp resonant peaks, which greatly depend on incident radiation angle and wavelength. From the numerical solution of the Maxwell equations, it was found that the sharp peaks have related solutions in the dispersion relation, explainable with the discrete-continuum coupling description. In their experiment, Crozier *et al.* [9] demonstrated that the resonances of an air-bridged photonic crystal slab exhibit considerable differences in their sensitivity according to the angle of illumination. Rosenberg *et al.* [12] showed that guided resonant modes can be readily observed in asymmetrical photonic crystal slabs built on high-index substrates. The guided resonant modes are found to give rise to strong high Q factor in the transmission spectra. Miroshnichenko *et al.* [13] demonstrated that high transmission through sharp bends in photonic crystal waveguides can be described by a simple model of the Fano resonance. Shanhui Fan *et al.* [6] showed that transmission and reflection of Fano resonance can be accounted by a simple Lorentzian resonance in the complex frequency plane.

One of the most popular simulation methods used for the present calculations consists in using the popular Finite-Difference Time-Domain (FDTD) algorithm joined with absorbing boundary conditions, usually known as Perfectly Matched Layer (PML). The excellence peculiarity of this method is the possibility to track the photon position to determine how the electromagnetic field will dislocate in the system. On the other hand, such a method presents the disadvantages of requiring huge amount of memory and long calculation time. An alternative approach, used in this paper, is to consider the Scattering Matrix Method (SMM) [14,15] that has the appreciable characteristic to avoid the mentioned drawbacks and, at the same time, to provide a reliable simulation for photonic crystal slabs.

In this paper, we will firstly extent the SMM to anisotropic materials, then we will apply it to investigate Fano resonance in general PhCS, and finally we will show how to control Fano modes in anisotropic materials.

2. Scattering Matrix Method in photonic crystal slabs

A commonly used representation of PhCS is shown in Fig. 1. The two dimensional periodicity is defined on the x - y plane, whereas in z direction uniformity is considered. Moreover, the electromagnetic field defining the system is assumed to have harmonic time dependence described by $\exp(-i\omega t)$. The Maxwell equations for anisotropic materials will then be expressed as,

$$\nabla \times \mathbf{E} = i\omega \mathbf{B}, \quad \nabla \times \mathbf{H} = -i\omega \mathbf{D}, \quad \nabla \cdot \mathbf{B} = 0, \quad \nabla \cdot \mathbf{D} = 0 \quad (1)$$

where $\mathbf{B}(\mathbf{r}) = \mu_0 \boldsymbol{\mu}(\mathbf{r}) \mathbf{H}(\mathbf{r})$ and $\mathbf{D}(\mathbf{r}) = \varepsilon_0 \boldsymbol{\varepsilon}(\mathbf{r}) \cdot \mathbf{E}(\mathbf{r})$. The quantities $\boldsymbol{\varepsilon}(\mathbf{r})$ and $\boldsymbol{\mu}(\mathbf{r})$ are the

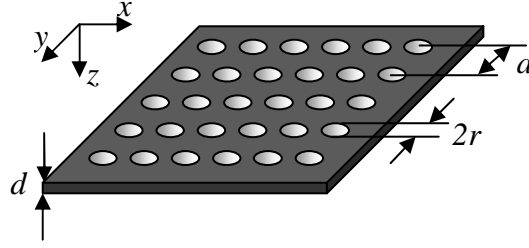


Fig. 1. Photonic crystal slab structure consisting of a square lattice of holes embedded into a uniform material.

relative dielectric constant and permeability, respectively. By defining the parallel components of the electric and magnetic field as $\mathbf{E}_{//} = (e_y, e_x)^T$ and $\mathbf{H}_{//} = (-h_x, h_y)^T$ [16], we can rewrite Eq. (1) as

$$\begin{aligned} -\frac{\partial}{\partial z} \mathbf{E}_{//} + \begin{pmatrix} \frac{\partial}{\partial y} \\ \frac{\partial}{\partial x} \end{pmatrix} e_z &= -i\omega\mu_0 \begin{pmatrix} \mu_{xx} & -\mu_{xy} \\ -\mu_{yx} & \mu_{yy} \end{pmatrix} \mathbf{H}_{//} + i\omega\mu_0 \begin{pmatrix} \mu_{xz} \\ -\mu_{yz} \end{pmatrix} h_z \\ \begin{pmatrix} \frac{\partial}{\partial x} & -\frac{\partial}{\partial y} \end{pmatrix} \mathbf{E}_{//} &= i\omega\mu_0 \begin{pmatrix} -\mu_{zx} & \mu_{zy} \end{pmatrix} \mathbf{H}_{//} + i\omega\mu_0 \mu_{zz} h_z \\ -\frac{\partial}{\partial z} \mathbf{H}_{//} + \begin{pmatrix} -\frac{\partial}{\partial x} \\ \frac{\partial}{\partial y} \end{pmatrix} h_z &= -i\omega\varepsilon_0 \begin{pmatrix} \varepsilon_{yy} & \varepsilon_{yx} \\ \varepsilon_{xy} & \varepsilon_{xx} \end{pmatrix} \mathbf{E}_{//} - i\omega\varepsilon_0 \begin{pmatrix} \varepsilon_{yz} \\ \varepsilon_{xz} \end{pmatrix} e_z \\ \begin{pmatrix} \frac{\partial}{\partial y} & \frac{\partial}{\partial x} \end{pmatrix} \mathbf{H}_{//} &= -i\omega\varepsilon_0 \begin{pmatrix} \varepsilon_{zy} & \varepsilon_{zx} \end{pmatrix} \mathbf{E}_{//} - i\omega\varepsilon_0 \varepsilon_{zz} e_z \end{aligned} \quad (2)$$

Once removed both \mathbf{E} and \mathbf{H} z-component from Eq. (2), we obtain:

$$\begin{aligned} \frac{\partial}{\partial z} \mathbf{H}_{//} + i\mathbf{F}^{(1)} \mathbf{H}_{//} &= \frac{ik_0}{\omega\mu_0} [\mathbf{F}^{(0)} \mathbf{E}_{//}] \\ \frac{\partial}{\partial z} \mathbf{E}_{//} + i\mathbf{T}^{(1)} \mathbf{E}_{//} &= \frac{i\omega\mu_0}{k_0} [\mathbf{T}^{(0)} \mathbf{H}_{//}] \end{aligned} \quad (3)$$

where

$$\begin{aligned} \hat{\mathbf{F}}^{(1)} &= -\begin{pmatrix} -\frac{\partial}{\partial x} \\ \frac{\partial}{\partial y} \end{pmatrix} \mu_{zz}^{-1} \begin{pmatrix} -\mu_{zx} & \mu_{zy} \end{pmatrix} - \begin{pmatrix} \varepsilon_{yz} \\ \varepsilon_{xz} \end{pmatrix} \varepsilon_{zz}^{-1} \begin{pmatrix} \frac{\partial}{\partial y} & \frac{\partial}{\partial x} \end{pmatrix} \\ \hat{\mathbf{T}}^{(0)} &= \begin{pmatrix} \varepsilon_{yy} & \varepsilon_{yx} \\ \varepsilon_{xy} & \varepsilon_{xx} \end{pmatrix} - \begin{pmatrix} \varepsilon_{yz} \\ \varepsilon_{xz} \end{pmatrix} \varepsilon_{zz}^{-1} \begin{pmatrix} \varepsilon_{zy} & \varepsilon_{zx} \end{pmatrix} - \begin{pmatrix} -\frac{\partial}{\partial x} \\ \frac{\partial}{\partial y} \end{pmatrix} \mu_{zz}^{-1} \begin{pmatrix} \frac{\partial}{\partial x} & -\frac{\partial}{\partial y} \end{pmatrix} \end{aligned}$$

$$\hat{\mathbf{T}}^{(1)} = - \begin{pmatrix} \mu_{xz} \\ -\mu_{yz} \end{pmatrix} \mu_{zz}^{-1} \begin{pmatrix} \frac{\partial}{\partial x} & -\frac{\partial}{\partial y} \end{pmatrix} - \begin{pmatrix} \frac{\partial}{\partial y} \\ \frac{\partial}{\partial x} \end{pmatrix} \epsilon_{zz}^{-1} \begin{pmatrix} \epsilon_{zy} & \epsilon_{zx} \end{pmatrix} \quad (4)$$

$$\hat{\mathbf{T}}^{(0)} = \begin{pmatrix} \mu_{xx} & -\mu_{xy} \\ -\mu_{yx} & \mu_{yy} \end{pmatrix} + \begin{pmatrix} \mu_{xz} \\ -\mu_{yz} \end{pmatrix} \mu_{zz}^{-1} \begin{pmatrix} -\mu_{zx} & \mu_{zy} \end{pmatrix} + \begin{pmatrix} \frac{\partial}{\partial y} \\ \frac{\partial}{\partial x} \end{pmatrix} \epsilon_{zz}^{-1} \begin{pmatrix} \frac{\partial}{\partial y} & \frac{\partial}{\partial x} \end{pmatrix}$$

Because of the structure periodicity, by using the Bloch theorem, the fields can be expanded as:

$$\begin{aligned} \mathbf{H}_{//}(\mathbf{r}) &= \sum_{\mathbf{G}} |\mathbf{k} + \mathbf{G}\rangle \mathbf{H}_{//}(\mathbf{G}) \exp(i\beta z) \\ \mathbf{E}_{//}(\mathbf{r}) &= \sum_{\mathbf{G}} |\mathbf{k} + \mathbf{G}\rangle \mathbf{E}_{//}(\mathbf{G}) \exp(i\beta z) \end{aligned} \quad (5)$$

being β the wave vector along z direction and $|\mathbf{k} + \mathbf{G}\rangle = \frac{1}{\sqrt{A}} \exp[i(\mathbf{k} + \mathbf{G}) \cdot \mathbf{r}]$. In the last expression \mathbf{k} is the wave vector in the lattice Brillouin zone, \mathbf{G} the reciprocal primitive lattice vector, \mathbf{r} the position vector in the x - y plane and A the area of the in-plane unit cell.

The relative dielectric constant $\epsilon(\mathbf{r})$ and permeability $\mu(\mathbf{r})$ are periodical tensors for the real space, so they can be express by means of Fourier series:

$$\begin{aligned} \epsilon(\mathbf{r}) &= \sum_{\mathbf{G}} \mathbf{V}_{\mathbf{G}} \exp[i(\mathbf{k} + \mathbf{G}) \cdot \mathbf{r}] \\ \mu(\mathbf{r}) &= \sum_{\mathbf{G}} \mathbf{U}_{\mathbf{G}} \exp[i(\mathbf{k} + \mathbf{G}) \cdot \mathbf{r}] \end{aligned} \quad (6)$$

where,

$$\begin{aligned} \mathbf{V}_{\mathbf{G}'-\mathbf{G}} &= \langle \mathbf{k} + \mathbf{G}' | \epsilon(\mathbf{r}) | \mathbf{k} + \mathbf{G} \rangle = V_{\mathbf{G}',\mathbf{G}} \\ \mathbf{U}_{\mathbf{G}'-\mathbf{G}} &= \langle \mathbf{k} + \mathbf{G}' | \mu(\mathbf{r}) | \mathbf{k} + \mathbf{G} \rangle = U_{\mathbf{G}',\mathbf{G}} \end{aligned} \quad (7)$$

Here the operator $\langle \circ | | \circ \rangle$ denotes integration in x - y plane on a unit cell domain. If \mathbf{P} and \mathbf{Q} are elements of either $\epsilon(\mathbf{r})$ or $\mu(\mathbf{r})$, natural extension of Eq. (7) results to be

$$\langle \mathbf{k} + \mathbf{G}' | \mathbf{PQ} | \mathbf{k} + \mathbf{G} \rangle = \sum_{\mathbf{G}''} \mathbf{P}_{\mathbf{G}',\mathbf{G}''} \cdot \mathbf{Q}_{\mathbf{G}'',\mathbf{G}} \quad (8)$$

Changing the Eq. (4) to matrix format:

$$\begin{aligned} \mathbf{F}^{(1)} &= \begin{pmatrix} \text{diag}(k_x + G_x) \\ -\text{diag}(k_y + G_y) \end{pmatrix} \mathbf{U}_{zz}^{-1} \begin{pmatrix} -\mathbf{U}_{zx} & \mathbf{U}_{zy} \end{pmatrix} + \begin{pmatrix} \mathbf{V}_{yz} \\ \mathbf{V}_{xz} \end{pmatrix} \mathbf{V}_{zz}^{-1} \begin{pmatrix} \text{diag}(k_y + G_y) & \text{diag}(k_x + G_x) \end{pmatrix} \\ \mathbf{F}^{(0)} &= \begin{pmatrix} \mathbf{V}_{yy} & \mathbf{V}_{yx} \\ \mathbf{V}_{xy} & \mathbf{V}_{xx} \end{pmatrix} - \begin{pmatrix} \mathbf{V}_{yz} \\ \mathbf{V}_{xz} \end{pmatrix} \mathbf{V}_{zz}^{-1} \begin{pmatrix} \mathbf{V}_{zy} & \mathbf{V}_{zx} \end{pmatrix} - \\ &\quad \begin{pmatrix} \text{diag}(k_x + G_x) \\ -\text{diag}(k_y + G_y) \end{pmatrix} \mathbf{U}_{zz}^{-1} \begin{pmatrix} \text{diag}(k_x + G_x) & -\text{diag}(k_y + G_y) \end{pmatrix} \end{aligned}$$

$$\begin{aligned}
\mathbf{T}^{(1)} &= \begin{pmatrix} \mathbf{U}_{xz} \\ -\mathbf{U}_{yz} \end{pmatrix} \mathbf{U}_{zz}^{-1} \begin{pmatrix} \text{diag}(k_x + G_x) & -\text{diag}(k_y + G_y) \end{pmatrix} + \begin{pmatrix} \text{diag}(k_y + G_y) \\ \text{diag}(k_x + G_x) \end{pmatrix} \mathbf{V}_{zz}^{-1} \begin{pmatrix} \mathbf{V}_{zy} & \mathbf{V}_{zx} \end{pmatrix} \\
\mathbf{T}^{(0)} &= \begin{pmatrix} \mathbf{U}_{xx} & -\mathbf{U}_{xy} \\ -\mathbf{U}_{yx} & \mathbf{U}_{yy} \end{pmatrix} + \begin{pmatrix} \mathbf{U}_{xz} \\ -\mathbf{U}_{yz} \end{pmatrix} \mathbf{U}_{zz}^{-1} \begin{pmatrix} -\mathbf{U}_{zx} & \mathbf{U}_{zy} \end{pmatrix} - \\
&\quad \begin{pmatrix} \text{diag}(k_y + G_y) \\ \text{diag}(k_x + G_x) \end{pmatrix} \mathbf{V}_{zz}^{-1} \begin{pmatrix} \text{diag}(k_y + G_y) & \text{diag}(k_x + G_x) \end{pmatrix}
\end{aligned} \tag{9}$$

Here *diag* represents a diagonal square matrix. By combining the previous relations we can get the parallel components of the electric and magnetic eigenfunctions in the reciprocal space:

$$\begin{aligned}
\mathbf{H}_{//}(\mathbf{G})\beta^2 + \left[\mathbf{F}^{(1)} + \mathbf{F}^{(0)}\mathbf{T}^{(1)}(\mathbf{F}^{(0)})^{-1} \right] \mathbf{H}_{//}(\mathbf{G})\beta + \left[\mathbf{F}^{(0)}\mathbf{T}^{(1)}(\mathbf{F}^{(0)})^{-1}\mathbf{F}^{(1)} - \mathbf{F}^{(0)}\mathbf{T}^{(0)} \right] \mathbf{H}_{//}(\mathbf{G}) &= \mathbf{O} \\
\mathbf{E}_{//}(\mathbf{G})\beta^2 + \left[\mathbf{T}^{(1)} + \mathbf{T}^{(0)}\mathbf{F}^{(1)}(\mathbf{T}^{(0)})^{-1} \right] \mathbf{E}_{//}(\mathbf{G})\beta + \left[\mathbf{T}^{(0)}\mathbf{F}^{(1)}(\mathbf{T}^{(0)})^{-1}\mathbf{T}^{(1)} - \mathbf{T}^{(0)}\mathbf{F}^{(0)} \right] \mathbf{E}_{//}(\mathbf{G}) &= \mathbf{O}
\end{aligned} \tag{10}$$

In several special situations, as for example in isotropic materials, dielectric and permeability tensors are constant quantities, hence $\mathbf{F}^{(1)} = \mathbf{T}^{(1)} = \mathbf{O}$. Under such hypothesis, Eq. (10) assumes a very simple form:

$$\begin{aligned}
\mathbf{H}_{//}(\mathbf{G})\beta^2 - \mathbf{F}^{(0)}\mathbf{T}^{(0)}\mathbf{H}_{//}(\mathbf{G}) &= \mathbf{O} \\
\mathbf{E}_{//}(\mathbf{G})\beta^2 - \mathbf{T}^{(0)}\mathbf{F}^{(0)}\mathbf{E}_{//}(\mathbf{G}) &= \mathbf{O}
\end{aligned} \tag{11}$$

where

$$\begin{aligned}
\mathbf{F}^{(0)} &= \begin{pmatrix} \mathbf{V} & \mathbf{O} \\ \mathbf{O} & \mathbf{V} \end{pmatrix} - \begin{pmatrix} \text{diag}(k_x + G_x) \\ -\text{diag}(k_y + G_y) \end{pmatrix} \mathbf{U}^{-1} \begin{pmatrix} \text{diag}(k_x + G_x) & -\text{diag}(k_y + G_y) \end{pmatrix} \\
\mathbf{T}^{(0)} &= \begin{pmatrix} \mathbf{U} & \mathbf{O} \\ \mathbf{O} & \mathbf{U} \end{pmatrix} - \begin{pmatrix} \text{diag}(k_y + G_y) \\ \text{diag}(k_x + G_x) \end{pmatrix} \mathbf{V}^{-1} \begin{pmatrix} \text{diag}(k_y + G_y) & \text{diag}(k_x + G_x) \end{pmatrix}
\end{aligned} \tag{12}$$

are written using the matrix formalism.

For anisotropic materials, when a critical direction is along *z* axis only, still $\mathbf{F}^{(1)} = \mathbf{T}^{(1)} = \mathbf{O}$. In this situation, $\mathbf{F}^{(0)}$ and $\mathbf{T}^{(0)}$ are described as:

$$\begin{aligned}
\mathbf{F}^{(0)} &= \begin{pmatrix} \mathbf{V}_{yy} & \mathbf{V}_{yx} \\ \mathbf{V}_{xy} & \mathbf{V}_{xx} \end{pmatrix} - \begin{pmatrix} \text{diag}(k_x + G_x) \\ -\text{diag}(k_y + G_y) \end{pmatrix} \mathbf{U}_{zz}^{-1} \begin{pmatrix} \text{diag}(k_x + G_x) & -\text{diag}(k_y + G_y) \end{pmatrix} \\
\mathbf{T}^{(0)} &= \begin{pmatrix} \mathbf{U}_{xx} & -\mathbf{U}_{xy} \\ -\mathbf{U}_{yx} & \mathbf{U}_{yy} \end{pmatrix} - \begin{pmatrix} \text{diag}(k_y + G_y) \\ \text{diag}(k_x + G_x) \end{pmatrix} \mathbf{V}_{zz}^{-1} \begin{pmatrix} \text{diag}(k_y + G_y) & \text{diag}(k_x + G_x) \end{pmatrix}
\end{aligned} \tag{13}$$

By solving the eigenvalue problems (10) for $\mathbf{E}_{//}(\mathbf{H}_{//})$, we get the elements of electric (magnetic) field in *x-y* plane. Then, by means of Eq. (3), we can easily recover the $\mathbf{H}_{//}(\mathbf{E}_{//})$ expression. Finally, we can express the fields as the sum of eigenfunctions:

$$\begin{aligned}\mathbf{H}_{//}(\mathbf{r}) &= \sum_{\mathbf{G},j} |\mathbf{k} + \mathbf{G}\rangle \left[\mathbf{H}_{//,j}^{(+)}(\mathbf{G}) a_j \exp(i\beta_j^{(+)} z) + \mathbf{H}_{//,j}^{(-)}(\mathbf{G}) b_j \exp(i\beta_j^{(-)} z) \right] \\ \mathbf{E}_{//}(\mathbf{r}) &= \sum_{\mathbf{G},j} |\mathbf{k} + \mathbf{G}\rangle \left[\mathbf{E}_{//,j}^{(+)}(\mathbf{G}) a_j \exp(i\beta_j^{(+)} z) + \mathbf{E}_{//,j}^{(-)}(\mathbf{G}) b_j \exp(i\beta_j^{(-)} z) \right]\end{aligned}\quad (14)$$

where (+) and (−) denote *quasi* forward and backward waves which are defined by the wave number β_j . When β_j is a real number, it is assumed to be positive for the (+) modes and negative for the (−) modes. If β_j is a complex number, the sign for the modes (+) and (−) is dictated by its imaginary part, similarly at the real case [15]. a_j and b_j are amplitude components of forward and backward waves, respectively.

At the interface, because of the electromagnetic boundary conditions, we have the relations:

$$\begin{pmatrix} \mathbf{E}_{//}^{(+)}(\mathbf{G}) & -\mathbf{E}_{//}^{(-)}(\mathbf{G}) \\ \mathbf{H}_{//}^{(+)}(\mathbf{G}) & -\mathbf{H}_{//}^{(-)}(\mathbf{G}) \end{pmatrix} \begin{pmatrix} \mathbf{a} \\ \mathbf{b}' \end{pmatrix} = \begin{pmatrix} -\mathbf{E}_{//}^{(-)}(\mathbf{G}) & \mathbf{E}_{//}^{(+)}(\mathbf{G}) \\ -\mathbf{H}_{//}^{(-)}(\mathbf{G}) & \mathbf{H}_{//}^{(+)}(\mathbf{G}) \end{pmatrix} \begin{pmatrix} \mathbf{b} \\ \mathbf{a}' \end{pmatrix}\quad (15)$$

We use the apex to denote the amplitude at other side of interface. The scattering matrix equation is defined as:

$$\mathbf{S} \begin{pmatrix} \mathbf{a} \\ \mathbf{b}' \end{pmatrix} = \begin{pmatrix} \mathbf{b} \\ \mathbf{a}' \end{pmatrix},$$

where,

$$\mathbf{S} = \begin{pmatrix} -\mathbf{E}_{//}^{(-)}(\mathbf{G}) & \mathbf{E}_{//}^{(+)}(\mathbf{G}) \\ -\mathbf{H}_{//}^{(-)}(\mathbf{G}) & \mathbf{H}_{//}^{(+)}(\mathbf{G}) \end{pmatrix}^{-1} \begin{pmatrix} \mathbf{E}_{//}^{(+)}(\mathbf{G}) & -\mathbf{E}_{//}^{(-)}(\mathbf{G}) \\ \mathbf{H}_{//}^{(+)}(\mathbf{G}) & -\mathbf{H}_{//}^{(-)}(\mathbf{G}) \end{pmatrix}\quad (16)$$

\mathbf{S} is the scattering matrix. The z component of the Poynting vector is $S_z = 1/2 \text{Re}(\mathbf{E}_{//}^*(\mathbf{r}) \times \mathbf{H}_{//}(\mathbf{r}))$, and it is a periodic function. However, we concern about the spatial average of the energy current in the plane. By integrating the quantity S_z on a unit cell, we obtain $S_z = 1/2 \text{Re}[\mathbf{E}_{//}^+(\mathbf{G}) \cdot \mathbf{H}_{//}(\mathbf{G})]$, where the superscript + represents the transpose-conjugate operation. In the end, the transmission and reflection are defined as $T = S_z^{\text{out}} / S_z^{\text{in}}$, $R = S_z^{\text{re}} / S_z^{\text{in}}$, respectively. Here, S_z^{in} , S_z^{re} and S_z^{out} are z components of Poynting vectors of incident, reflection and transmission light, respectively.

The number of plane waves utilized in the simulations presented in this paper oscillates between 81 and 197. For example, in Fig. 2 we have used 197 plane waves. Because the main goal of this paper is to show the possibility to control Fano's resonances, we believe that a further increment of plane waves cannot give us any more knowledge about the simulated systems.

We want to conclude this section pointing out that even though the method so far described was utilized to calculate one-layer PhCS structure, there are nor conceptual neither practical limitations to its application to multiple-layer devices.

3. Fano resonance in isotropic photonic crystal slabs

In this section, we will apply the SMM to analyze the light Fano resonance effect in two dimensional PhCS.

3.1 Fano resonance modes

The PhCS described in this section is fabricated by c-Si with holes filled by SiO₂ and insert in a sandwich of SiO₂. The thickness of the slab is $0.5a$, the radius of the holes is $0.15a$, and a is the lattice constant. Throughout this paper, our model will consist of a square lattice. The refractive index of c-Si and SiO₂ is 3.5 and 1.46, respectively. Relative permittivity is 1. We neglect any frequency dependence of Si and SiO₂ dielectric function. Light is incident along z direction which implies polarization degeneration. The transmission is shown at the top side of Fig. 2.

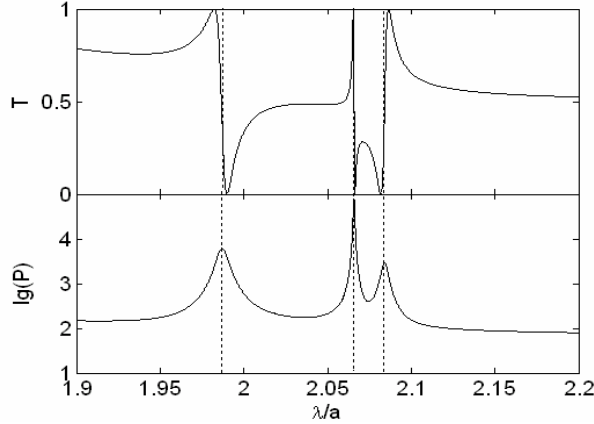


Fig. 2. Three Fano's resonances at $1.9871a$, $2.0658a$ and $2.0841a$ are shown. In particular, the top graph shows the variation of transmission in the wavelength region from $1.9a$ to $2.2a$. The bottom graph shows the energy P calculated in a unit cell of PhCS. The energy peaks correspond to wavelength values roughly in between $T=0$ and $T=1$.

In the wavelength region of $1.9\sim 2.2 a$ are present three Fano's resonances. Each of them lives in a very narrow wavelength region, where the transmission changes greatly up to the maximum theoretical value of 1. The Fano resonance phenomenon is manifested by the presence of a discrete state coupled with a continuum of states. The continuum of states corresponding to the background transmission [5], are the states of Si film without PhC structure. The discrete states are confined by SiO₂ poles and Si film. The lower part of Fig. 2 shows the curve of energy P for a unit cell of Si layer versus wavelength. It is defined by the relation

$$P = \int_{cell} \frac{1}{2} (\mathbf{D}^* \cdot \mathbf{E} + \mathbf{B}^* \cdot \mathbf{H}) dV \quad (17)$$

Because P is proportional to the energy stored in the cavity, it implies direct proportion with the quality factor Q . The constant relating the two quantities is defined by the amplitude of the electric field. The peaks of energy indicate Fano resonances. They prove the presence of a discrete state in correspondence of the maximum of curve P . In Ref. [31] were found very interesting phenomena related to the asymmetry of Fano's resonance. In particular, was concluded that the main feature of Fano resonance is the resonant reflection but not transmission. We have then tried to investigate further the difference between transmission deeps and peaks relating them to the energy distribution shown in Fig. 2. Unluckily, no clear relation was possible to obtain so that no definitive conclusion was reached. Anyway, we have to notice that the number of plane waves (197) utilized for the current simulation does not guarantee absolute convergence. Such a value is definitely enough for the general purposes of this paper, but probably not in finding a precise relation between transmission and energy distribution.

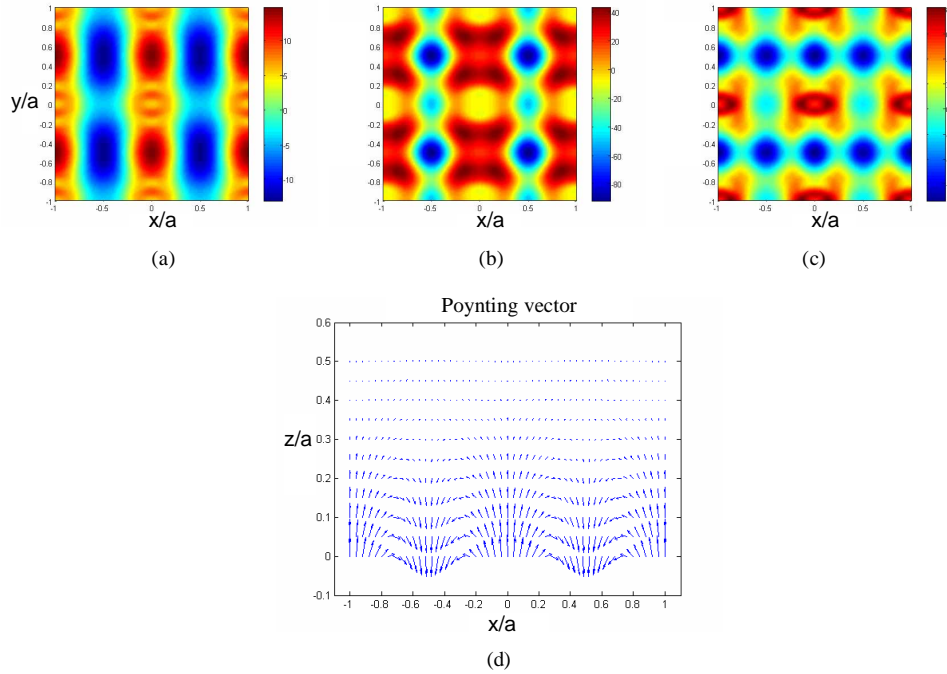


Fig. 3. (a), (b) and (c) show the S_z distribution for each Fano resonance of Fig (2). The patterns cover four unit cells, which have a hole just in the center. (d) Distribution of the Poynting vector at the plane $y/a=0.5$, $z \geq 0$.

The z polarization distribution of the Poynting vector at top interface plane is shown in Fig. 3(a), (b), and (c). The SiO_2 pole is just at the center of the images. They correspond to the three peaks shown in Fig. 2. The scale in Fig. 3(b) highlights the presence of a sharp field distribution. It is because of the strong resonant electromagnetic field inside the cell. The periodic behavior of the Poynting vector is shown in Fig. 3(d). It is a section of half plane at $y/a = 0.5$, $z \geq 0$ in Fig. 3(a). Even though the energy current shows a double behavior, namely it travels along both positive and negative directions, for any cross section along z axis the total energy current remains positive. It is also evident how the periodicity is primarily stressed close to the surface. This is because the light in PhCS is not transmitted just along the z direction, but it consists of many contributes with $\mathbf{G} + \beta \hat{\mathbf{z}}$ wave number. For such a reason, some of them are reflected at the interface. However, light is able to penetrate deeply in SiO_2 material.

Figure 4(a) shows the transmission spectrum for incoming light belonging to the x - z plane. The horizontal line indicates the incidence angle whereas the ordinate represents the wavelength. $\theta=0$ corresponds to the incident beam parallel to the z axis. In the reciprocal space, scanning the incident angle from 0° to 80° means to look along ΓX direction. The top and the bottom graphs show s - and p -polarization, respectively. As expected, for acclivitous oblique incident light, the transmission spectrum starts depending strongly on the light polarization. This is because of the polarization degeneration breakdown due to the component of the \mathbf{k} vector parallel to the x - y plane. When the angle θ is far from zero, such component is different from zero too, hence it can be shown that the two polarizations are not degenerate anymore. It is interesting to notice how a single Fano mode becomes, by tuning the wavelength, a continue line which from now on will be defined as *characteristic line*. It is indeed a peculiarity of the investigated system.

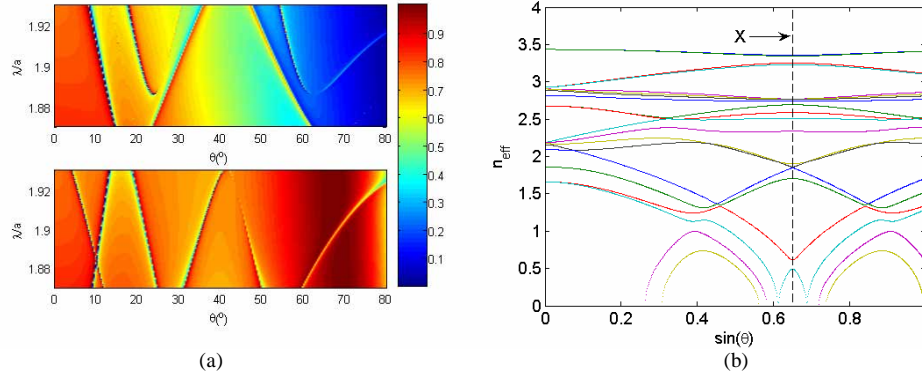


Fig. 4. (a) Transmission spectrum of the incident light for s (top) and p (bottom) polarization. The incoming angle θ is from 0° to 80° , where zero means a beam parallel to the z axis. Narrow Fano resonances form several characteristic lines. (b) Relation between n_{eff} and incident light angle. Light is along ΓX direction. The dashed line denotes the X point, beyond which the mirror effect for n_{eff} is shown.

As previously shown, the energy is mainly confined inside the slab. It is because of the high Q-factor related to the quasi-guided mode, that manifests itself by means of Fano's resonance. It explains why Fano resonance states are also called *quasiguide mode* [7]. Indeed, they are very similar to a guide mode in photonic crystal slab [8]. At the same time, the characteristic lines denote the photonic crystal slab band structure in the real space [10,11]. Figure 4(b) remarks the interconnection between the z and in-plane components of the k vector. Indeed, because of both momentum conservation and slab periodicity, they are intimately related. In particular, the graph shows in ordinate the effective refractive index along z direction, $n_{\text{eff}} = \beta/k_0$, and in abscissa the high symmetry direction ΓX defined in k space, where $\sin(\theta) = k_x/k$. Here $k_0 = 2\pi/\lambda$, being λ the wavelength of the incident light. When k_x exceeds the X point, the corresponding modes move to the contiguous Brillouin zone, so to realize a symmetric response.

3.2 Controlling Fano resonance region by varying the slab refractive index

Interesting and useful applications can derive from the capability in controlling the Fano resonance wavelength. Indeed, because we can design very narrow Fano resonant regions, the possibility to change rapidly transmission (or reflection) is obtained by minor shifts of the wavelength. The tool which allows us to modify the wavelength position comes from tuning the PhCS index. Such operation on Si can be actuated by carriers injection [17]. This method is already applied in optical crystal switches [18] and M-Z modulators [5].

Fig. 5(a) shows the transmission and reflection spectra at $\theta=0$ with the Si refractive index being tuned at different frequencies. It is evident that Fano resonance peaks move to shorter wavelengths by decreasing the Si refractive index. Same behavior is present in PhC too, in fact when a reduction of the mean refractive index occurs the bands shift to higher frequency regions. Figure 5(b) illustrates the transmission (reflection) variation ΔT (ΔR) when acting on the refractive index and wavelength. Its analytical expression assumes the form $\Delta T = T(n_0 + \Delta n) - T(n_0)$, n_0 is refractive index of Si. Of course, when $\Delta n = 0$, also the transmission variation must be equal to zero, as shown in the image. Beside it, fixed the wavelength at Fano resonance values, it is possible to get transmission (reflection) variations close to one. The narrower is the Fano peak, the more sensitive is the answer of the system. Such characteristic can be applied for the realization of optical switches. Moreover, the line width of Fano resonance modes depends on the coupling grade between discrete and continuum states. The weaker is

the coupling, the narrower is the line width. However, the coupling strength can be controlled by the filling ratio of the materials. For example, by reducing the radius of the holes, the line width ends up to be narrower (See Fig. 12 in Ref. [6]).

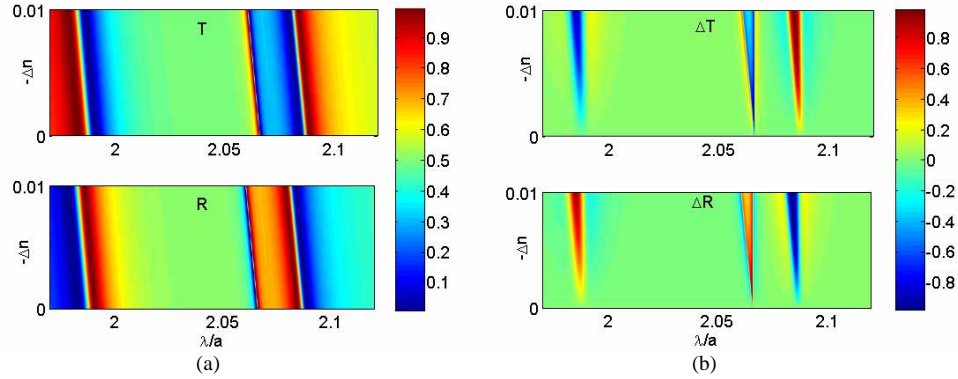


Fig. 5. (a) Transmission and reflection spectra calculated at $\theta=0$. The sharp lines show Fano resonances. The reduction of Si refractive index shifts the resonance lines to shorter wavelengths. (b) Transmission and reflection variation spectra. ΔT and ΔR are defined as $T(n_0+\Delta n)-T(n_0)$ and $R(n_0+\Delta n)-R(n_0)$. At Fano wavelengths strong changes of T and R are possible. Variation range of Si index is from 0 to -0.01. The range of wavelength is from $1.97a$ to $2.12a$.

3.3 Enhancement of the first order scattered light: Wood's resonant effects

PhCS are grating structures. Inside of them light follows different paths, so that reflection and transmission result from their combination. The number of scattered beams is in relation with both the lattice constant and the refractive index of the slab materials. Indeed, because of the periodicity of the system, some requirements regarding the light propagation must be satisfied. In particular, in material composed by uniform and periodic structures, by means of the Bloch theorem results $(\mathbf{k}_{\parallel} + \mathbf{G})^2 + k_z^2 = k^2$, $\mathbf{G} = m\mathbf{G}_1 + n\mathbf{G}_2$, being k_{\parallel} defined on x - y plane, and \mathbf{G} the reciprocal primitive space vector. Such equivalence is determined by both the lattice constants (G_1 and G_2) and the refractive index of materials ($k=nk_0$).

In Figs. 6 we fix the wavelength at $1.5a$, with the incident light on the x - z plane. The electric field is assumed to have y polarization. The 0^{th} (S_0) and 1^{st} (S_1) orders of the scattered light are shown. A scanning of Si refractive index n was performed. In particular values of Δn from -0.001 to -0.009 were chosen. Abscissa shows the incident light angle θ . Dot and solid lines represent 0^{th} and 1^{st} order scattered light, respectively. When the refractive index variation is equal to -0.005 and incident angle around 20.8° , the transmitted light -Fig. 6(b)- is almost fully associated with S_1 mode. Moreover, the light direction is along $-x$ axis, giving the false impression of negative refraction. In reality, the coupling between the first order of the scattered light with the quasi-guide modes and the Rayleigh phenomenon are responsible for such effect [19-33]. Evident high sensibility results from the simulations. In fact, small changes of either refractive index or incidence angle produce different light distributions.

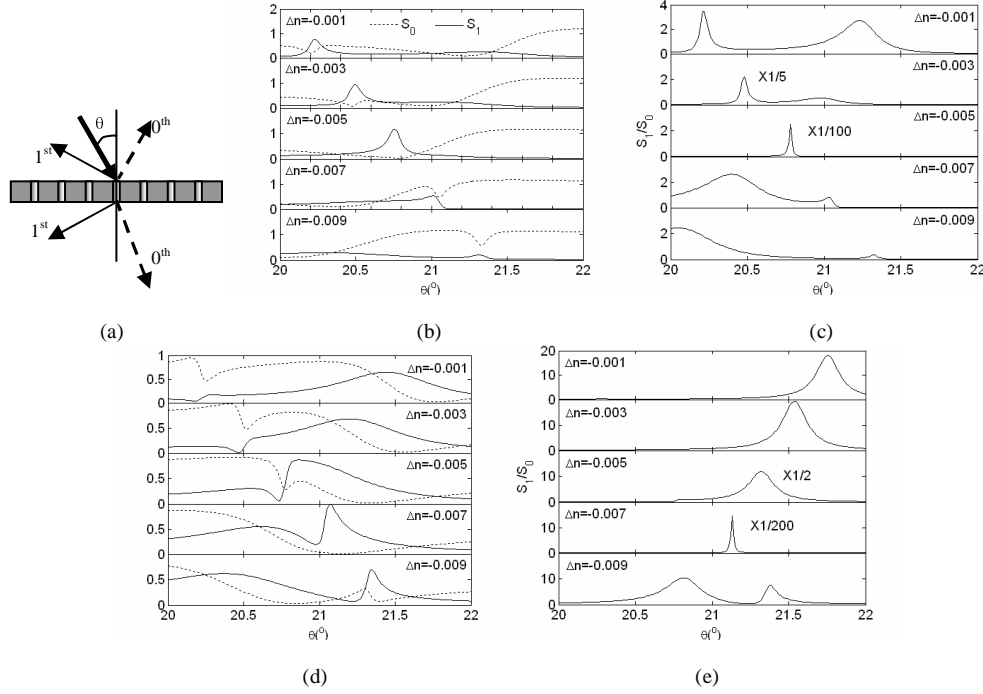


Fig. 6. (a) Sketch of 0th and 1st order scattered light directions. Incident light, 0th, and 1st order scattered light are denoted by heavy, dot and thin line, respectively. (b) Power flux spectrum of 0th and 1st order transmitted light. Dot and solid lines represent 0th and 1st order transmitted light, respectively. (c) Power flux ratio between 1st and 0th order transmitted light. (d) and (e) describe the reflection case. Figs. (b), (c), (d) and (e) consist of five graphs each, corresponding to variations of Si refractive index in the interval [-0.001, -0.009].

Figure 6(c) shows the ratio of transmitted light amplitude between the 1st and 0th order Poynting vectors. Maximum ratio value is approximately 250. It has strong dependence on the 0th order S_0 . Indeed, looking for example at the first graph in Fig. 6(c), two peaks emerge. They correspond to the two S_0 minimum in Fig. 6(b). The two peaks move vis-à-vis by increasing Δn . The reflection spectra are shown in Fig. 6(d) & (e). The maximum ratio between the 1st and the 0th order reflected Poynting vectors occurs at $\Delta n = -0.007$ and incident light angle equal to 21.15°.

4. Light transport in anisotropic photonic crystal slabs

In section III we have shown Fano resonance modes in Si/SiO₂ isotropic PhCS and how to control them by acting on the slab refractive index. In this section we will give an example, KTP (Potassium Titanium Oxide Phosphate), to show how the Fano resonance modes can be controlled inside anisotropic materials.

4.1 Transmission spectrum of KTP anisotropic PhCS

KTP is a well known anisotropic material. The dielectric constant is depicted as function of both wavelength and temperature [34]:

$$n_i^2(\lambda, T) = a_i + \beta_i(T^2 - 400) + \frac{b_i + \delta_i(T^2 - 400)}{\lambda^2 - c_i + \phi_i(T^2 - 400)} - \lambda^2 [d_i + \rho_i(T^2 - 400)] \quad (18)$$

where $i=1,2,3$. Each i value defines an element of the dielectric constant tensor $\varepsilon = \begin{pmatrix} \varepsilon_1 & 0 & 0 \\ 0 & \varepsilon_3 & 0 \\ 0 & 0 & \varepsilon_2 \end{pmatrix}$. Here ε_1 , ε_2 and ε_3 are parallel to x , z and y direction, respectively.

All the coefficients appearing in Eq. (18) are the same as in [34].

The structure is made out of KTP and follows the pattern of Fig. 1. The air holes have diameter $0.3\mu\text{m}$, lattice constant is $1.0\mu\text{m}$, slab thickness $0.6\mu\text{m}$ and insert in a sandwich of SiO_2 . The incident light is assumed to be parallel to the z axis. Because of the transversal property of the electromagnetic waves, both \mathbf{E} and \mathbf{H} belong to the x - y plane.

Be ϕ the angle between \mathbf{E} and x axis. Figure 7 shows transmission (top) and reflection (bottom) depending both on ϕ and the wavelength λ of the incident light. When the angle is zero, meaning polarization along x axis, two strong Fano resonances are present. Increasing the angle increases the number of Fano modes too, up to the maximum of four at $\phi=45^\circ$. At the same time their intensity decreases. This situation corresponds to \mathbf{E} being in between x and y axis. A further increase of ϕ , up to 90° , re-establish the original situation of two sharp Fano resonances but shifted in frequency respect to the case $\mathbf{E} // x$. From 90° to 180° symmetrical behavior is shown. In the end, Fig. 7 seems to show that the sharpest Fano modes do exist when the electric field is parallel either to x or to y axis.

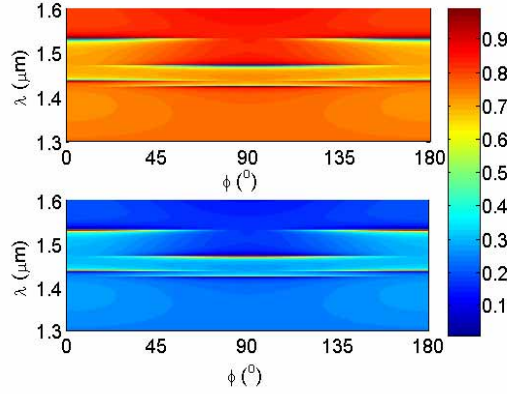


Fig. 7. Transmission (top) and reflection (bottom) spectra for different incident polarizations. ϕ is the angle between electric field angle and x axis.

Figures 8(a) and (b) show the dependence of Fano wavelengths on temperature for $1\mu\text{m}$ thick KTP slab. The graphs are associated to light polarization along y and x directions, respectively. Each graph consists of ten curves which denote the temperature increase from 20°C to 200°C . Fano resonances move along the wavelength axis when the temperature is increased. The dot line traces the Fano resonance behavior on the wavelength-temperature plane. By plotting the Fano resonant wavelength λ_F^2 versus T^2-400 , as indicated in Fig. 9, a linear behavior is obtained. The curves analytical expression is $\lambda_F^2 = \lambda_0^2 + \eta(T^2 - 400)$, where $\lambda_0 = 1.6311$, $\eta = 4.98127 \times 10^{-7}$ for s -polarization ($E // x$ - y plane), and $\lambda_0 = 1.6278$, $\eta = 5.1744 \times 10^{-7}$ for p -polarization ($E // x$ - z plane). λ_F is the Fano resonance wavelength. Such a behavior is consistent with the results of Fig. 5, where linear relation between refractive index and wavelength is shown in the case of isotropic PhC slab. Indeed, according to Eq. (18), refractive index is proportional to temperature, namely there is a direct proportion between refractive index and wavelength for KTP slabs too.

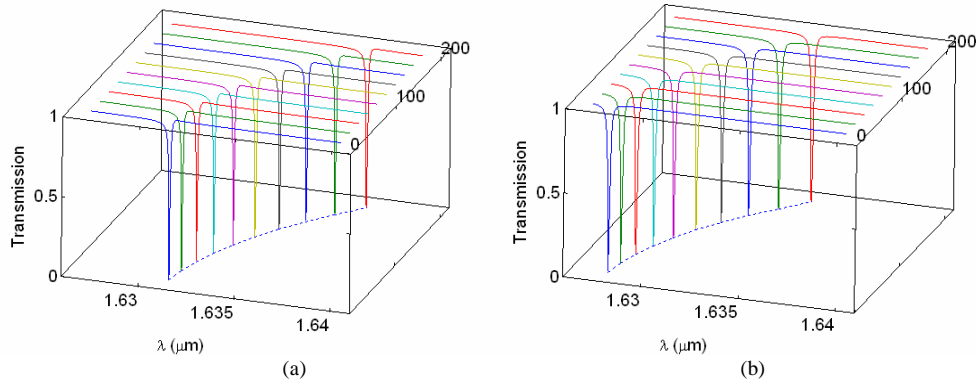


Fig. 8. (a) and (b) show transmission spectra at varies temperatures for $E//y$ and $E//x$, respectively. The differences are due to the anisotropic nature of KTP. Each graph consists of ten curves. Temperature is increased from 20°C to 200°C with constant steps of 20°C. The dot line shows the relation between Fano resonance wavelengths and temperature.

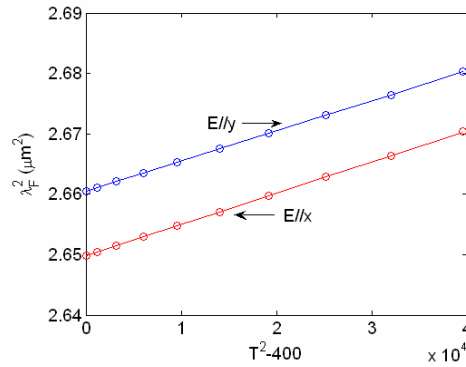


Fig. 9. Fano resonant wavelength λ_f versus temperature. The graph shows linear dependence of λ_f^2 with T^2 , namely linear relation between λ_f and temperature. In abscissa is plotted T^2-400 to be consistent with Eq. 18.

5. Conclusion

We have presented an approach for the extension of the Scattering Matrix Method to describe the optical behavior of anisotropic materials. Such a method was utilized to investigate Fano resonances in Photonic Crystal Slabs (PhCS). It was shown that in a situation of Fano resonance, Fano resonant modes present narrow line width.

The Fano wavelength shift is polarization independent. However, it can be obtained acting on the slab refractive index. For example, the refractive index of Si can be changed by electrons injection. When the Fano wavelength shift occurs, transmission and reflection spectra shift occur too. We have found that appreciable wavelength variations are possible for small refractive index change ($\Delta n = -0.01$). Also the scattering light can be controlled. The process is so efficient that only the 1st order scattering contribute can be selected. Interesting, such a contribute looks like negative refraction. For anisotropic materials, Fano resonant wavelength shift is still polarization independent. The example of KTP crystal was introduced. It is defined by a refractive index which is temperature sensitive. In particular, in our structure, the Fano resonances steps-up to longer wavelengths by increasing the temperature. Because of

its sensitivity, KTP can be utilized for applications where high definition temperature control is an issue.

Acknowledgments

The authors thank Prof. F. Rossi at Politecnico of Turin, Italy for beneficial and useful discussions. Financial support by the Opening Project of State Key Laboratory on Integrated Optoelectronics of China is gratefully acknowledged.